

# AMI observations of northern supernova remnants at 14–18 GHz<sup>\*</sup>

AMI Consortium: Natasha Hurley-Walker<sup>†</sup>, A. M. M. Scaife, D. A. Green, Matthew L. Davies, Keith Grainge, Michael P. Hobson, Michael E. Jones<sup>‡</sup>, Tak Kaneko, Anthony Lasenby, Guy Pooley, Richard D. E. Saunders, Paul F. Scott, David Titterton, Elizabeth Waldram and Jonathan T. L. Zwart

*Astrophysics Group, Cavendish Laboratory, Cambridge University, 19 J. J. Thomson Avenue, Cambridge CB3 0HE*

*<sup>‡</sup> Astrophysics, Oxford University, Keble Road, Oxford OX1 3RH*

Accepted —; received —; in original form 10 March 2022

## ABSTRACT

We present observations between 14.2 and 17.9 GHz of 12 reported supernova remnants (SNRs) made with the Arcminute Microkelvin Imager Small Array (AMI SA). In conjunction with data from the literature at lower radio frequencies, we determine spectra of these objects. For well-studied SNRs (Cas A, Tycho’s SNR, 3C58 and the Crab Nebula), the results are in good agreement with spectra based on previous results. For the less well-studied remnants the AMI SA observations provide higher-frequency radio observations than previously available, and better constrain their radio spectra. The AMI SA results confirm a spectral turnover at  $\simeq 11$  GHz for the filled-centre remnant G74.9+1.2. We also see a possible steepening of the spectrum of the filled-centre remnant G54.1+0.3 within the AMI SA frequency band compared with lower frequencies. We confirm that G84.9+0.5, which had previously been identified as a SNR, is rather an HII region and has a flat radio spectrum.

**Key words:** supernova remnants – radio continuum: ISM – radiation mechanisms: non-thermal

## 1 INTRODUCTION

We present observations of 12 reported supernova remnants (SNRs) selected from the 2006 version of Green’s SNR catalogue<sup>1</sup> made with the Arcminute Microkelvin Imager Small Array (AMI SA, see Kneissl et al. 2001 and AMI Consortium: Zwart et al. 2008) at 14.2 to 17.9 GHz. The integrated flux densities from the AMI SA observations are used in conjunction with measurements from the literature to investigate the synchrotron spectrum of these remnants. There are few observations of Galactic SNRs at frequencies above 10 GHz, and several issues can be addressed by observing at higher frequencies. Generally, observations over a wide range of frequencies are essential to investigate energy injection and loss processes in the intergalactic medium. More specifically, ‘filled-centre’ remnants have relatively flat, non-thermal spectra, with spectral indices  $\alpha$  typically between 0.0 and 0.3 (here we define  $\alpha$  such that flux density  $S$  varies with frequency  $\nu$  as  $S \propto \nu^{-\alpha}$ ). Such flat spectra steepen at high frequencies; the positions of features such as spectral breaks, when known, vary considerably between different remnants (e.g. Morsi & Reich 1987; Salter et al. 1989; Green &

Scheuer 1992; Bock & Gaensler 2005). In the case of several filled-centre remnants the frequency of the turnover is not yet known. Also, there have been suggestions (Reynolds & Ellison 1992; Tian & Leahy 2005; Urošević, Pannuti & Leahy 2007, see also Tian & Leahy 2006) that ‘shell’ type remnants, which typically have  $\alpha$  in the range 0.3 to 0.7, show spectral flattening at higher frequencies. However, the detection of small changes in spectral index over a limited range of frequencies is not easy (see e.g. Green 2007), and observations over a wider range of frequencies is an advantage in such studies. Finally, possible excess ‘anomalous’ emission – which may be from spinning dust – has been reported in the case of one Galactic SNR (3C396, AMI Consortium: Scaife et al. 2007). These AMI SA observations provide additional constraints on any similar emission associated with the observed remnants.

## 2 THE TELESCOPE

The AMI SA is situated at the Mullard Radio Astronomy Observatory, Cambridge. It consists of ten 3.7-m-diameter equatorially-mounted dishes with a baseline range of  $\simeq 5$ –20 m. The telescope observes in the band 12–18 GHz with cryogenically-cooled indium-phosphide HEMT front-end amplifiers. The system temperature is typically about 25 K. The astronomical signal is mixed with a 24-GHz local-oscillator signal to produce an intermediate-frequency signal of 6–12 GHz. The correlator is an analogue

<sup>\*</sup> We request that any reference to this paper cites “AMI Consortium: Hurley-Walker et al. 2009”

<sup>†</sup> Issuing author: email – nh313@mrao.cam.ac.uk

<sup>1</sup> <http://www.mrao.cam.ac.uk/surveys/snrs/>; see also Green (2004).

**Table 2.** Assumed I + Q flux densities of 3C286 and 3C48, and errors on flux measurements in each frequency channel, over the commonly used AMI SA bandwidth.

Channel	$\bar{\nu}$ /GHz	$S^{3C286}$ /Jy	$S^{3C48}$ /Jy	$\sigma_s$
3	14.24	3.61	1.73	3.0%
4	14.96	3.49	1.65	2.3%
5	15.68	3.37	1.57	1.9%
6	16.41	3.26	1.49	2.1%
7	17.13	3.16	1.43	1.7%
8	17.86	3.06	1.37	3.4%

Fourier transform spectrometer with 16 correlations formed for each baseline at path delays spaced by approximately 26 mm. From these correlations, the complex signals in each of eight channels of 750 MHz bandwidth are synthesized. Note that for correlators of this type, the synthesized channels are correlated at the  $\approx 10$  per cent level. In practice, the lowest two frequency channels are presently unused due to a low response in this frequency range, and interference from geostationary satellites. The FWHM of the primary beam of the AMI SA is  $\approx 20'$  at 16 GHz and the FWHM of its synthesised beam is at minimum  $\approx 2'$ . The average synthesised beam for a map made with combined frequency channels is shown in the figures presented in this paper, and is an effective measure of the resolution.

### 3 OBSERVATIONS

Observations of 12 reported SNRs (see Table 1) were made with the AMI SA during the period June–July 2007. These targets were selected from Green’s SNR catalogue on the basis of angular diameter ( $\leq 12'$ , to be mapped in a single pointing) and declination ( $\delta > 18^\circ$ , to be accessible, given the hardware constraints at the time). The sample of SNRs includes several bright, well-studied objects in the Galactic anti-centre: G111.7–2.1 (=Cas A), G120.1+1.4 (=Tycho’s SNR), G130.7+3.1 (=3C58) and G184.6–5.8 (=Crab Nebula). Comparison of AMI SA maps, flux densities and spectra of these objects with data from the literature provides a useful verification of the performance of the telescope. The sample also includes less well studied objects, and indeed one has recently been revealed by Foster et al. (2007) as an HII region rather than a SNR (see further discussion of G84.9+0.5 below). The positions and effective thermal noise associated with each AMI SA observation are shown in Table 1; note that the noise levels for the brighter objects are limited by the dynamic range available. The observations were typically eight hours long and used interleaved observations of bright, nearby point sources at hourly intervals for phase calibration. The sensitivity of AMI SA over all baselines, all channels, is  $\approx 30$  mJy  $s^{-1/2}$  giving  $\approx 0.2$  mJy after eight hours. Given that the objects observed here are bright, eight hours is more than sufficient to obtain accurate flux densities; however the long observations are important to produce good maps, whose structure is dependent on the  $uv$  coverage.

### 4 CALIBRATION AND DATA REDUCTION

Data reduction was performed using the local software tool REDUCE, developed from the VSA data-reduction software of the same name. This applies appropriate path compensator and path delay corrections, flags interference, shadowing and hardware errors, applies phase and amplitude calibrations and Fourier transforms the

correlator data readout to synthesize the frequency channels, before output to disk in  $uv$  FITS format suitable for imaging in AIPS.

Flux calibration was performed using short observations of 3C48 and 3C286 near the beginning and end of each run, with assumed I + Q flux densities for these sources in the AMI SA channels consistent with Baars et al. (1977) (see Table 2). As Baars et al. (1977) measure I and AMI SA measures I + Q, these flux densities include corrections for the polarization of the sources derived by interpolating from VLA 5-, 8- and 22-GHz observations.

Secondary calibrators were selected from the Jodrell Bank VLA Survey (JVAS; Patnaik et al. 1992; Browne et al. 1998; Wilkinson et al. 1998) on the basis of their declination and flux density (see Table 3). Over one hour, the phase is generally stable to  $5^\circ$  for channels 4–7, and  $10^\circ$  for channels 3 and 8.

The system temperature is continuously monitored using a modulated noise signal injected at each antenna; this ‘rain gauge’ is used to continuously correct the amplitude scale in a frequency-independent way. The overall consistency of the flux density scale is estimated to be better than 5 per cent.

The reduced visibility data were imaged using AIPS. Maps were made from both combined channel datasets – for channels 3 to 8 inclusive – shown in this paper, and from individual channels. The broad spectral coverage of AMI SA allows a representation of the spectrum between 14 and 18 GHz to be made.

Since the AMI SA antennas are sensitive to a single linear polarization (I+Q) and are equatorially mounted, this polarization is fixed on the sky during the observation; therefore, the intensity of polarised sources may be under- or overestimated. However, for the integrated flux densities, this is not expected to be more than 10 per cent, which is comparable to the quoted (statistical) uncertainties. For example, Boland et al. (1966) obtain integrated percentage polarizations of  $\approx 9$  per cent and  $\approx 1$  per cent at 15 GHz for the Crab Nebula and Cas A respectively. While some SNR have large polarization on small scales, the AMI SA observations integrate over the whole source so this effect is reduced. Errors on the AMI SA data points were estimated by combining the contributions of several sources of error:

- Thermal noise on each channel and the dynamic range limit give rms map noise  $\sigma_{\text{rms}}$ ;
- error on flux calibration (including rain gauge correction) of  $\approx 3$  per cent (see Table 2);
- we increase the flux calibration error to 10 per cent in the case of those sources which undergo flux loss correction;
- estimate of flux using tilted-plane method: changes in fitting area result in  $\leq 1$  per cent changes in amplitude.

Thus the overall error was estimated as  $\sigma = \sqrt{(\sigma_{\text{rms}}^2 + [0.03 \text{ or } 0.10] S_i)^2}$ .

Spectra were compiled from the flux densities presented here in conjunction with those available in the literature. Power-law spectra were fitted to these data using a Gaussian likelihood function and Markov Chain Monte Carlo (MCMC) (Metropolis et al. 1953) sampling technique. This method is much faster than the traditional parameter estimation methods and provides an error estimate on the spectral index directly from the posterior parameter distribution. The resulting spectral indices are given in Tables 4 and 12.

The correlation between AMI SA channels mentioned in Section 2 is internal to AMI SA dataset, so its effect on the spectral fit to AMI SA data and that from the literature is minimal.

**Table 1.** Our SNR sample. Names are of the form G[galactic longitude]±[galactic latitude]. Column 4 contains the effective thermal noise for the AMI SA observation of each object. Column 6 denotes the type of SNR: S = shell-type, F = filled-centre, ? = unclear. Positions, angular sizes and types are from Green’s catalogue, with angular size for G59.5+0.1 corrected (see text).

Name	$\alpha$ (J2000)	$\delta$ (J2000)	$\sigma_{\text{th}}$ (mJy beam <sup>-1</sup> )	$\theta$ arcmin	Type	Common name
G54.1+0.3	19 30 31	+18 52	0.52	1.5	S	
G57.2+0.8	19 34 59	+21 57	0.17	12	S?	
G59.5+0.1	19 42 33	+23 35	0.48	5	S	
G63.7+1.1	19 47 52	+27 45	0.19	8	F	
G67.7+1.8	19 54 32	+31 29	0.22	9	S	
G74.9+1.2	20 16 02	+37 12	0.84	8 × 6	F	
G76.9+1.0	20 22 20	+38 43	0.17	12 × 9	?	
G84.9+0.5 <sup>a</sup>	20 50 30	+44 53	0.32	6	S	
G111.7–2.1	23 23 26	+58 48	92.0	5	S	Cas A
G120.1+1.4	00 25 18	+64 09	2.9	8	S	Tycho’s SNR
G130.7+3.1	02 05 41	+64 49	14	9 × 5	F	3C58
G184.6–5.8	05 34 31	+22 01	165	7 × 5	F	Crab Nebula

<sup>a</sup>HII Region; see text.

**Table 3.** Phase calibrators used during SNR observations. 16-GHz flux densities were measured with AMI SA.

Source	$\alpha$ (J2000)	$\delta$ (J2000)	$S_{16}^{\text{AMISA}}/\text{Jy}$	SNR calibrated
J1925+2106	19 25 59.6	+21 06 26	2.15	G54.1+0.3, G57.2+0.8, G59.5+0.1, G63.7+1.1
J2007+404	20 07 44.9	+40 29 49	2.09	G67.7+1.8, G74.9+1.2, G76.9+1.0
J2052+365	20 52 52.1	+36 35 35	1.17	G84.9+0.5
J2355+498	23 55 09.5	+49 50 08	1.01	G111.7–2.1
J0019+734	00 19 45.8	+73 27 30	2.05	G120.1+1.4
J0217+738	02 17 30.8	+73 49 33	3.38	G130.7+3.1
J0530+1331	05 30 56.4	+13 31 55	4.53	G184.6–5.8

## 5 RESULTS AND DISCUSSION

Deriving accurate flux densities for extended objects in the Galactic plane, such as SNRs, is not straightforward. In the majority of remnants presented here we have adopted the fitting method of Green (2007). In this method a flux density is estimated by drawing a polygon around the SNR and fitting a tilted plane to the pixels around the edges of the polygon. The tilted plane is then removed from the image before integrating the emission within the polygon. Where there is a bright source closely adjacent to the SNR, such as in the case of G74.9+1.2, the dividing line between the SNR and adjacent source is omitted in fitting the plane. It was found that the flux density varied by less than 1 per cent with different fitting regions; a contribution for this error is included in the error on each flux density derived using this method.

As an interferometric telescope AMI SA does not measure total power and therefore will lose flux on different angular scales depending on the individual  $uv$  coverage towards each source. Where total power maps are publically available, it is possible to quantify the amount of flux loss in the AMI SA data, or indeed any interferometric data, subject to the assumption that the morphology of the region is unchanged between the frequency of the total power map and that of the interferometer. In this paper the flux loss inherent in each AMI SA channel towards the sources G67.7+1.8, G74.9+1.2, G76.9+1.0, G84.9+0.5, G120.1+1.4, and G130.7+3.1 has been calculated by sampling the Fourier transform of the total power maps from the Canadian Galactic Plane Survey (CGPS; Kothes et al. 2006) archives at 1.4 GHz to match the  $uv$  coverage of the corresponding AMI observation. The remainder of our SNR sample is not yet covered by the publically available CGPS data and the same method cannot be applied. In the case of G63.7+1.1, where we be-

lieve flux loss to be important, we have calculated a percentage loss for each channel using a Gaussian model for the source and sampling it appropriately. In the cases of those sources that have not been corrected for flux loss, the importance of this is discussed in the notes on individual sources.

### 5.1 Well-studied SNR

There are several SNR in the northern sky that have been extensively studied at a wide range of frequencies. We compared flux densities from the literature with those derived from AMI SA data in order to examine the calibration of the telescope. The AMI SA flux densities for each channel are given in Table 4. Two SNRs (G120.1+1.4 and G130.7+3.1) are structurally extended and the measured AMI flux densities are corrected for flux loss resulting from changing  $uv$  coverage over our frequency band. The other two SNRs (G111.7–2.1 and G184.6–5.8) are less extended and flux loss has a less significant effect on the AMI flux densities. We do not give a flux density averaged over the combined bandwidth of AMI SA because of it is very large. Instead, we provide an interpolated value for the midpoint of AMI’s bandpass (after flux loss correction, where appropriate).

**G111.7–2.1, Cassiopeia A** (Fig. 1). This is the brightest known Galactic ‘shell’ SNR, and is well studied at all wavelengths, with its absolute spectrum being the basis of the radio flux density scale established by Baars et al. (1977). The structure of Cas A is barely resolved by the AMI SA observations.

The absolute radio spectrum of Cas A follows a power-law, with  $\alpha = 0.79$  (for epoch 1965.0), from 300 MHz to 31 GHz. Since Cas A is a relatively young SNR, only about 300 years old (see e.g. Stephenson & Green 2002), its flux density shows a significant

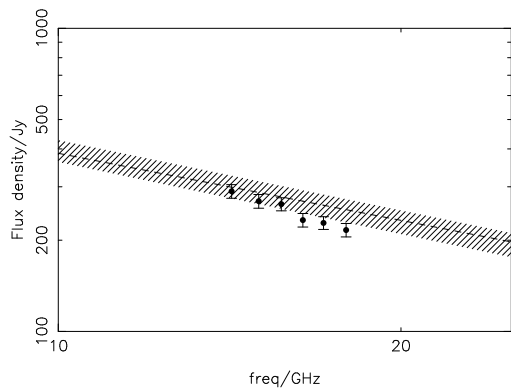
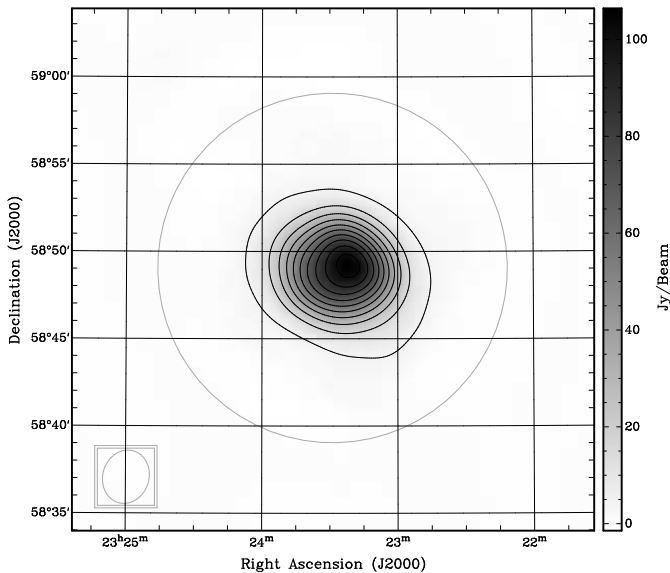


**Figure 1.** Above: Map of G111.7–2.1 (Cassiopeia A). AMI SA 16-GHz contours and greyscale image. Contours are linear percentage levels from 5% to 95% in steps of 10%. The peak level is  $106 \text{ Jy beam}^{-1}$ . Here, and throughout this paper, the large grey circle indicates the average FWHM of the primary beam, i.e. where the apparent flux density falls to 50%; also, the ellipse in the bottom-left corner indicates the half-maximum of the synthesized beam; this gives a measure of the resolution of the AMI SA images. In this, and all images including AMI SA data, the top six channels comprising a bandwidth of 5.7 GHz have been combined; 16 GHz refers to the central frequency. Below: Radio spectrum of G111.7–2.1. Data points are from the AMI SA and the dashed line shows a spectrum fitted to data taken from the literature (including a correction for secular decay); the hatching indicates the error on the fit ( $\alpha = 0.81 \pm 0.01$ ).

secular decrease. Baars et al. constructed their absolute spectrum for Cas A by bringing the available absolute flux density measurements to a common epoch, 1965.0, using a frequency-dependent secular decrease of

$$\frac{1}{S} \frac{dS}{dt} = 0.97(\pm 0.04) - 0.30(\pm 0.04) \log\left(\frac{\nu}{\text{GHz}}\right) \text{ per cent yr}^{-1}, \quad (1)$$

i.e. a rate of  $0.61 \text{ per cent yr}^{-1}$  at 16 GHz. From the 1965.0-epoch spectrum of Cas A, the predicted flux density at 16 GHz, epoch 2007.5, is  $275 \pm 18 \text{ Jy}$  (assuming an exponential decay at the annual rate given by eq. 1), which is in reasonable agreement with the value obtained with AMI:  $256 \pm 25 \text{ Jy}$ . The polarisation of Cas A is only 1 per cent at 15 GHz so this is not expected to affect the measured flux density significantly.

**G120.1+1.4, Tycho’s SNR** (Fig. 2). This is a shell remnant which

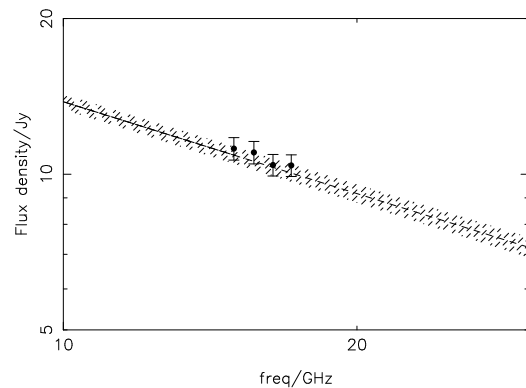
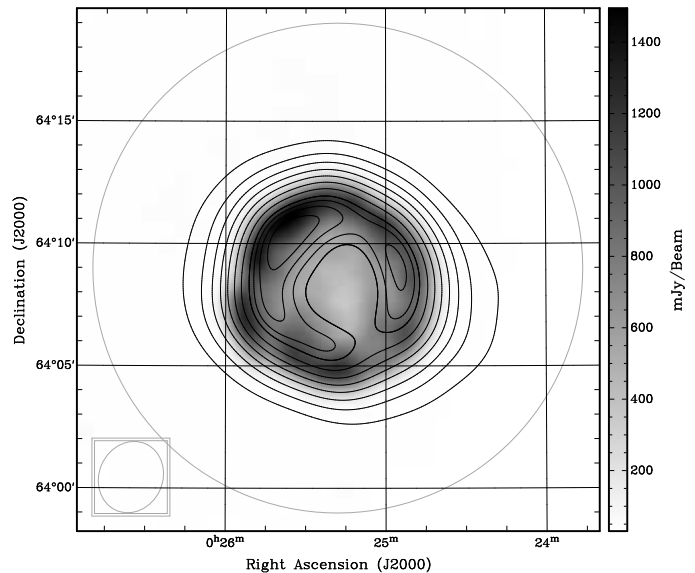


**Figure 2.** Above: Map of G120.1+1.4 (Tycho’s SNR). AMI SA 16-GHz contours are overlaid on a CGPS 1.4-GHz greyscale image. Contours are linear percentage levels from 10% to 80% in steps of 10%, and from 80% to 100% in steps of 5%, in order to highlight the shell structure. The peak level is  $1.16 \text{ Jy beam}^{-1}$ . Annotations are as in Fig. 1. Below: Radio spectrum of G120.1+1.4. Data points are from the AMI SA and the dashed line shows a spectrum fitted to data taken from the literature; the hatching indicates the error on the fit ( $\alpha = 0.58 \pm 0.01$ ).

is clearly resolved by the AMI SA observations. The shell is brighter to the north-east, in agreement with lower-frequency observations (e.g. Katz-Stone et al. 2000). After correction for flux loss, the flux densities from the AMI SA observations are in good agreement with the known radio spectrum of G120.1+1.4 (see Fig. 2). The interpolated value of the flux density at 16 GHz,  $10.8 \pm 1.1 \text{ Jy}$ , is within the error bars of the predicted value at 16 GHz,  $10.5 \pm 0.5 \text{ Jy}$ .

**G130.7+3.1, 3C58** (Fig. 3). This ‘filled-centre’ SNR may be the remnant of the historical supernova of AD 1181 (see e.g. Stephenson & Green 2002), although this association is not universally accepted (see e.g. Fesen 2008). G130.7+3.1 is extended east-west and is known to have a relatively flat radio spectrum, with  $\alpha \approx 0.09$  up to frequencies of at least several tens of gigahertz (e.g. Green 1986; Salter et al. 1989), but the position of its spectral turnover is not known (Green & Scheuer 1992). The AMI SA integrated flux densities, after correction for flux loss, are in reasonable agreement with published flux densities of 3C58 (e.g. Green 1986). For instance, our interpolated value of the flux den-

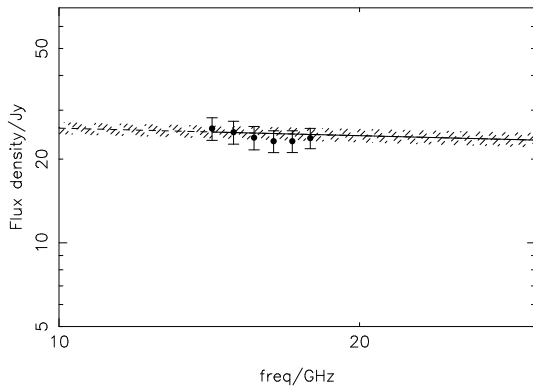
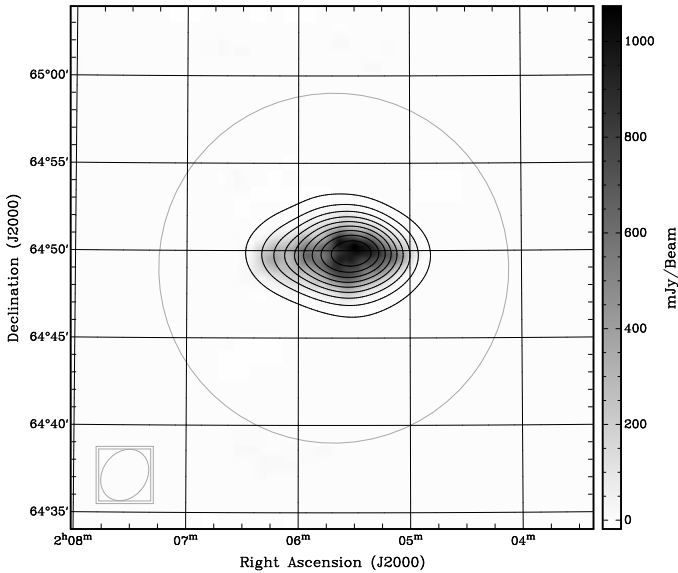


**Figure 3.** Above: Map of G130.7+3.1 (3C58). AMI SA 16-GHz contours are overlaid on a NRAO VLA Sky Survey (NVSS; Condon et al. 1998) 1.4-GHz greyscale image. Contours are linear percentage levels from 10% to 100% in steps of 10%. The peak level is  $8.48 \text{ Jy beam}^{-1}$ . Annotations are as in Fig. 1. Below: Radio spectrum of G130.7+3.1. Data points are from the AMI SA and the dashed line shows a spectrum fitted to data taken from the literature; the hatching indicates the error on the fit ( $\alpha = 0.09 \pm 0.01$ ).

sity at 16 GHz,  $23.1 \pm 2.3 \text{ Jy}$ , agrees well with the predicted value at 16 GHz,  $25.0 \pm 1.1 \text{ Jy}$ .

**G184.6–5.8, the Crab Nebula** (Fig. 4). The spectrum of the Crab Nebula is well known, showing a power-law behaviour over a wide range of radio frequencies (e.g. Baars et al. 1977) with  $\alpha = 0.30$ , with a secular decrease of  $\approx 0.17 \text{ per cent yr}^{-1}$  (Aller & Reynolds 1985, see also Vinyaikin 2007). Recent observations by Green, Tuffs & Popescu (2004) also show that the Crab Nebula has a very similar structure from 1.4 to 345 GHz, consistent with a simple, single synchrotron spectral power-law between these frequencies. We note that the Crab Nebula has  $\approx 9 \text{ per cent}$  integrated polarization at 15 GHz (Boland et al. 1966), at a position angle of  $140^\circ$ . For these integrated polarization parameters, the observed I + Q flux density will overestimate the true flux density by about 3.5 per cent, so a correction of this magnitude has been made to the AMI flux densities listed in Table 4.

We assume a decrease in flux density of 7 per cent over the 40 years since the absolute flux density measurements used for Baars et al.’s spectrum, based on a decrease of  $\sim 0.17 \text{ per cent yr}^{-1}$ . Taking this into account, the integrated flux densities from the AMI SA

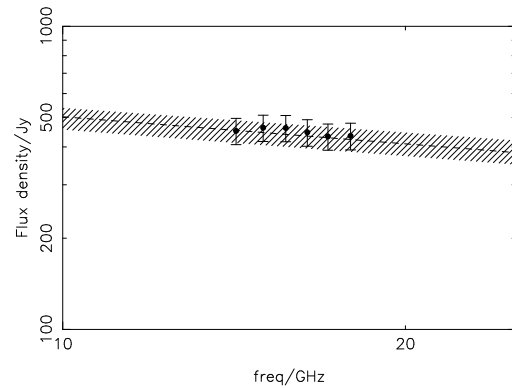
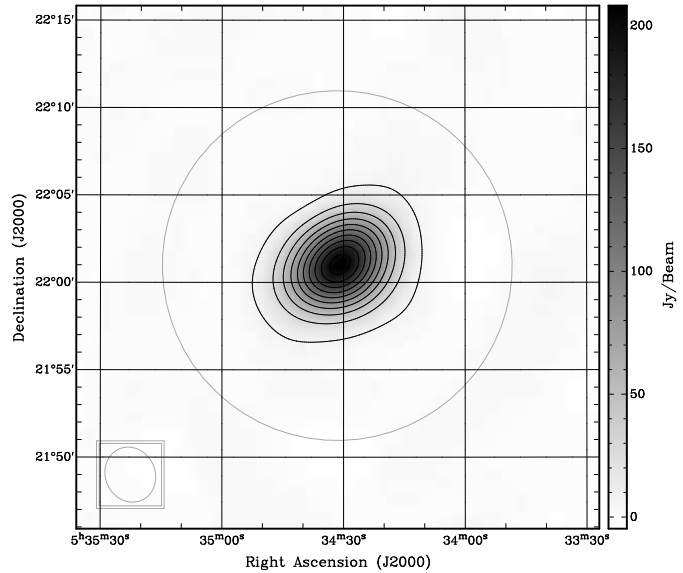


**Figure 4.** Above: Map of G184.6–5.8 (Crab Nebula). AMI SA 16-GHz contour and greyscale image. Contours and annotations are as in Fig. 3. The peak level is  $208 \text{ Jy beam}^{-1}$ . Below: Radio spectrum of G184.6–5.8. Data points are from the AMI SA and the dashed line shows a spectrum fitted to data taken from the literature (including a correction for secular decay); the hatching indicates the error on the fit ( $\alpha = 0.294 \pm 0.002$ ).

observations are in good agreement with the results expected from extrapolation of the results of Baars et al.. For comparison, an interpolated value of the measured flux density at 16 GHz is  $450 \pm 45 \text{ Jy}$ , compared to an predicted value of  $424 \pm 33 \text{ Jy}$ . This object has not been flux-loss corrected but as it is relatively compact, this is not expected to be a large effect.

## 5.2 Other SNRs at 16 GHz

These SNRs are less well-studied and most have not been observed at frequencies greater than 10 GHz so high frequency data from AMI SA are of particular interest. We present short notes on each SNR and derive spectral indices (shown in the captions to each image) from a combination of AMI SA data and flux densities from the literature at lower frequencies, using the method described in Section 4. Some exceptions are made: G59.5+0.1 has too complicated a structure to reliably fit to, and G74.9+1.2 has a spectral break at 11 GHz, so the fit is only made to data below this frequency.

**G54.1+0.3** (Fig. 5). This is a small filled-centre remnant for which

**Table 4.** AMI SA I+Q flux densities of well-studied SNR. Above: corrected for flux loss, where possible; below: original flux densities for those sources which undergo a flux loss correction.

Name	Freq. /GHz					
	14.2 (Jy)	15.0 (Jy)	15.7 (Jy)	16.4 (Jy)	17.1 (Jy)	17.9 (Jy)
G111-7-2.1 <sup>a</sup>	290 ± 29	269 ± 27	263 ± 26	233 ± 23	228 ± 23	216 ± 22
G120-1+1.4 <sup>b</sup>	–	11.2 ± 0.6	11.0 ± 0.6	10.4 ± 0.5	10.4 ± 0.5	–
G130-7+3.1 <sup>b</sup>	25.8 ± 2.4	25.0 ± 2.4	23.9 ± 2.3	23.2 ± 2.1	23.2 ± 2.1	23.8 ± 1.2
G184-6-5.8 <sup>a</sup>	452 ± 45	463 ± 46	462 ± 46	447 ± 45	433 ± 43	435 ± 44
G120-1+1.4	–	10.3 ± 0.3	9.8 ± 0.3	8.8 ± 0.2	7.7 ± 0.2	–
G130-7+3.1	24.7 ± 1.2	24.3 ± 1.2	23.4 ± 1.1	21.8 ± 1.0	21.2 ± 1.0	22.4 ± 1.1

<sup>a</sup>Uncorrected for flux loss; no CGPS coverage.<sup>b</sup>Corrected for flux loss using CGPS data.**Table 5.** Integrated flux densities from the literature for G54-1+0.3.

v/GHz	S <sub>i</sub> /mJy	Reference
0.327	495 ± 75	Velusamy & Becker (1988)
0.327	504 ± 17	Taylor et al. (1996)
1.4	478 ± 30	Velusamy & Becker (1988)
1.4	327.5 ± 10.9	Condon, Broderick & Seielstad (1989)
1.42	364 ± 36	Caswell & Haynes (1987)
1.6	417 ± 30	Velusamy & Becker (1988)
2.7	580 ± 60	Reich et al. (1984)
4.75	370 ± 40	Reich et al. (1985)
4.8	325 ± 20	Velusamy & Becker (1988)
4.875	400 ± 40	Altenhoff et al. (1979)
5.0	306 ± 31	Griffith et al. (1990)
10.7	263 ± 30	This work, from the data of Handa et al. (1987)

there are no published radio flux densities at frequencies above 5 GHz, so the position of any possible spectral break is not yet known. We derive an integrated flux density at 10 GHz from the data of Handa et al. (1987). Three ‘arms’ of extended emission surround the remnant and are obvious in both the 2.7-GHz data of the Effelsberg 11-cm survey (Reich et al. 1984; Fürst et al. 1990) and in infra-red emission seen in the IRAS 100- $\mu$ m image. To the south-east a large HII region (e.g. Chini, Kruegel & Wargau (1987)) can be seen which, like the ‘arms’, is well-traced by the IRAS 100  $\mu$ m data. This background morphology makes fitting the flux density of G54-1+0.3 difficult as can be seen by the scatter in the flux density data from the literature – see Table 5. The AMI SA observations indicate a steeper spectrum than at lower frequencies, however the reliability of this result is brought into question by the varying background on different angular scales which may affect the flux densities and lead to an artificially steep spectrum. In an attempt to assess this effect the data from each AMI SA channel were truncated to a common *uv* range. This produced a similar spectrum across the AMI SA band, suggesting that the steepening is indeed genuine. However, in order to provide a definite answer observations at higher frequencies are required.

**G57-2+0.8** (Fig. 6). This remnant has not previously been studied at frequencies above 5 GHz. In the AMI SA band it appears to have a teardrop-shaped emission limb of peak flux 0.09 Jy beam<sup>-1</sup> at 16 GHz. This SNR is not associated with PSR1937+214, which is more than 1 degree away. The AMI SA flux densities have not been flux corrected as there is no CGPS coverage at this position. This may explain the observed slightly lower fluxes and the apparent steepening of the spectrum across the AMI band compared to the extrapolated spectrum from low frequencies.

**G59-5+0.1** (Fig. 7). The AMI SA observation of G59-5+0.1 is dominated by a bright HII region (e.g. Lockman 1989) which lies

**Table 6.** Integrated flux densities from the literature for G57-2+0.8.

v/GHz	S <sub>i</sub> /Jy	Reference
0.083	8.0 ± 2.0	Kovalenko, Pynzar & Udal'tsov (1994)
0.178	4.0 ± 1.0	Caswell & Haynes (1987)
0.327	3.2 ± 0.1	Taylor et al. (1996)
1.4	1.29 ± 0.13	White & Becker (1992)
1.42	1.43 ± 0.14	Fürst et al. (1990)
1.42	1.34 ± 0.10	Sieber & Seiradakis (1984)
2.7	0.90 ± 0.09	Reich et al. (1984)
2.7	0.86 ± 0.10	Sieber & Seiradakis (1984)
3.9	0.8 ± 0.1	Trushkin, Vitkoskij & Nizhelskij (1987)
4.85	0.618 ± 0.062	Becker, White & Edwards (1991)
4.85	0.642 ± 0.023	Gregory et al. (1996)
4.85	0.64 ± 0.02	Taylor et al. (1996)

to the north of the SNR. In order to produce a better image of the SNR, the HII region was observed separately. The HII region was then CLEANED and the CLEAN components (scaled for the primary beam) subtracted from the original G59-5+0.1 visibility data. These data were then re-mapped and CLEANED using NVSS and Westerbork Synthesis Radio Telescope (WSRT) 327-MHz data (Taylor, Wallace & Goss 1992) as a reference, to produce the image shown in Fig. 7. As the AMI SA's beam reaches a null at 40' from the pointing centre, the HII region S86 (Lockman 1989) is revealed only as a small limb to the southeast. We confirm that G59-5+0.1 is a shell-type SNR with the ‘barrel-like’ morphology described by Taylor et al. (1996): brighter in the SW and NE. The flux in the SE is contaminated with an extragalactic source as detected by NVSS. The slight NW extension is also influenced by a point source. It is difficult to image north of  $\delta = 23^\circ 45'$  as the subtraction of the HII region is imperfect and may have left artefacts.

Taylor et al. (1996) measure the flux density of G59-5+0.1 to be 5.07 ± 0.16 Jy at 327 MHz and < 1.65 Jy at 4.85 GHz, suggesting a spectral index of greater than  $\alpha = 0.41$ . This would imply a flux density of  $\leq 1$  Jy at 16 GHz. From the AMI SA combined channel map, see Fig. 7, we measure a flux density of  $S_i = 0.146 \pm 0.015$  Jy, where the error has been estimated as  $\sigma = \sqrt{\sigma_{\text{th}}^2 + (0.1S_i)^2}$ . A 10 per cent error on the flux density is used here since the integrated flux density is highly dependent on the defined fitting region. Although the SNR catalogue of Green (2004) lists the angular size of G59-5+0.1 to be 5', this is an error, as Taylor et al. (1996) measure the extent of this source to be 15', a size which is consistent with the emission seen at 16 GHz by AMI SA. We do not list the AMI SA flux densities for individual channels as the complex nature of the region makes flux loss estimates unreliable. This prevents us from fitting a spectrum to the measured flux densities since for a source of such angular extent and distinct

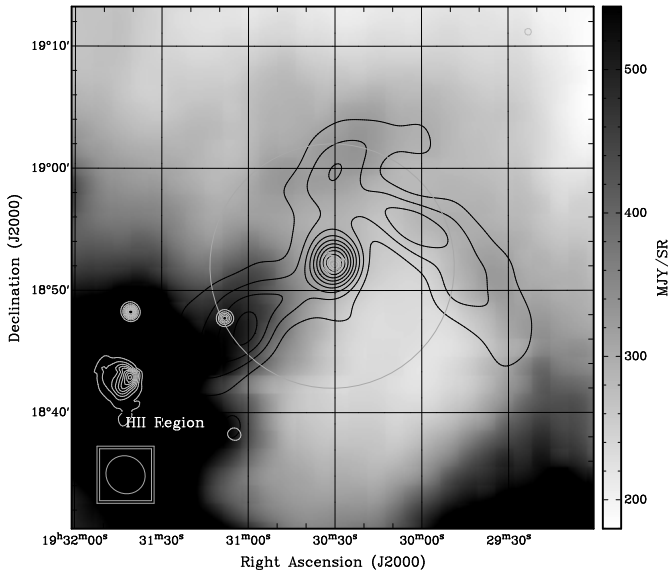


**Figure 5.** Above: Map of G54.1+0.3. AMI SA 16-GHz contours (black) and NVSS 1.4-GHz contours (grey) are overlaid on a IRAS 100- $\mu\text{m}$  greyscale image. The peak level of the AMI SA contours is  $0.21 \text{ mJy beam}^{-1}$  and the peak level of the NVSS contours is  $389 \text{ mJy beam}^{-1}$ . Contours and annotations are as in Fig. 3. Below: Radio spectrum of G54.1+0.3. Integrated flux densities taken from the literature (Table 5) are shown as crosses, and those from AMI SA (Table 12) are shown as filled circles. The best-fitting power-law, with  $\alpha = 0.14$ , is shown as a dashed line.

substructure the losses will not only be large, but will also differ significantly between channels.

**G63.7+1.1** (Fig. 8). The AMI SA observation shows this to be a relatively featureless object. The integrated flux densities listed here, see Table 7, include the flux from two nearby compact sources which are unresolved in AMI SA and earlier observations (Wallace, Landecker & Taylor 1997). The AMI SA flux densities are consistent with the spectrum extrapolated from lower frequencies.

**G67.7+1.8** (Fig. 9). This remnant has a double arc structure, confused with an extragalactic point source near  $19^{\text{h}}54^{\text{m}}15^{\text{s}}$ ,  $+31^{\circ}30'45''$ . The AMI SA flux densities are in good agreement with extrapolation from the available lower frequency flux densities.

**G74.9+1.2** (Fig. 10). This is a filled-centre remnant, with a nearby flat-spectrum extragalactic source. At lower radio frequencies this remnant has a relatively flat spectrum, with  $\alpha = 0.26$ , with observations from Morsi & Reich (1987) and Salter et al. (1989) implying a spectral break at around 11 GHz, i.e. at a frequency just below the

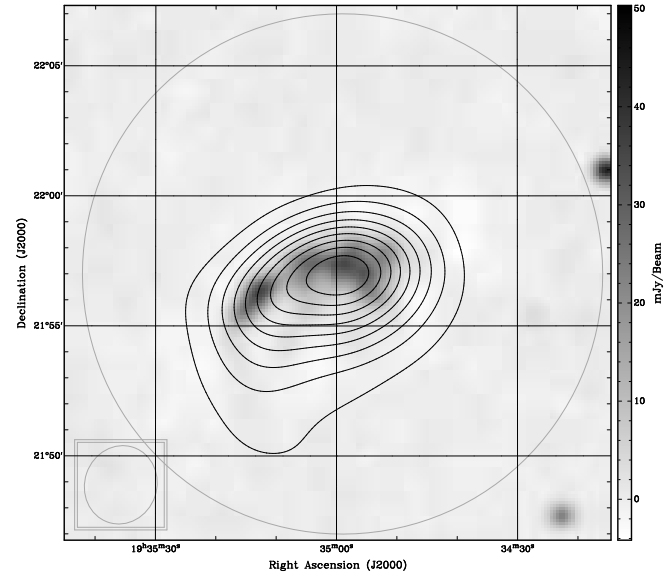


**Figure 6.** Above: Map of the G57.2+0.8 region. AMI SA 16-GHz contours are overlaid on a NVSS 1.4-GHz greyscale image. Contours and annotations are as in Fig. 3. The peak level is  $92.0 \text{ mJy beam}^{-1}$ . Below: Radio spectrum of G57.2+0.8. Integrated flux densities taken from the literature (Table 6) are shown as crosses, and those from AMI SA (Table 12) are shown as filled circles. The best-fitting power-law, with  $\alpha = 0.67$ , is shown as a dashed line.

AMI SA band. The AMI SA flux densities are indeed less than the expected values from a simple extrapolation from lower frequencies, in agreement with the 14.35-GHz flux density from Langston et al. (2000).

**G76.9+1.0** (Fig. 11). This is an extended, polarised radio source in the Galactic plane, with a non-thermal spectrum. It was first interpreted as a probable SNR by Landecker, Higgs & Wendker (1993), similar to G65.7+1.2 (=DA 495, e.g. Landecker & Caswell 1983). It is  $9' \times 12'$  in extent, with diffuse emission surrounding two lobes. Landecker, Higgs & Wendker (1993) propose that this is a ‘filled-centre’ remnant, with a spectral break at relatively low frequencies, explaining their measurement of the non-thermal spectrum with  $\alpha \approx 0.62$  at higher frequencies. Subsequently Landecker et al. (1997) suggested that the spectral break is at  $\approx 1$  GHz. The AMI SA results are consistent with the non-thermal spectrum seen from other observations above  $\approx 1$  GHz.

**G84.9+0.5** (Fig. 12). This was identified as a SNR by Taylor et al. (1996), using data at 327 MHz from the WSRT and at 4850 MHz from Condon, Broderick & Seielstad (1989). However, recent observations at 408 and 1420 MHz from the CGPS have indicated a

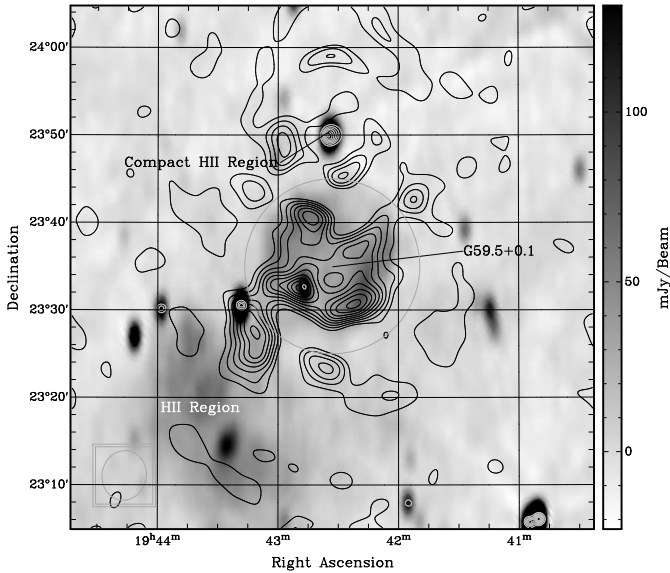


**Figure 7.** Above: Map of G59.5+0.1. AMI SA 16-GHz contours (black) and NVSS 1.4-GHz contours (grey) are overlaid on a WSRT 327-MHz greyscale image. The peak level of the AMI SA contours is  $18.8 \text{ mJy beam}^{-1}$  and the peak level of the NVSS contours is  $417 \text{ mJy beam}^{-1}$ . The north compact HII region has been subtracted from the AMI SA data to enhance the image of G59.5+0.1. Contours and annotations are as in Fig. 3.

**Table 7.** Integrated flux densities from the literature for G63.7+1.1.

$\nu/\text{GHz}$	$S_i/\text{Jy}$	Reference
0.327	$2.47 \pm 0.25$	Taylor et al. (1996)
0.408	$2.1 \pm 0.2$	Wallace, Landecker & Taylor (1997)
1.39	$1.76 \pm 0.01$	Wallace, Landecker & Taylor (1997)
1.42	$1.71 \pm 0.02$	Wallace, Landecker & Taylor (1997)
1.42	$1.62 \pm 0.16$	Fürst et al. (1990)
1.42	$1.34 \pm 0.1$	Sieber & Seiradakis (1984)
2.695	$1.5 \pm 0.15$	Reich et al. (1984)
2.695	$1.41 \pm 0.1$	Wallace, Landecker & Taylor (1997)
4.85	$1.147 \pm 0.115$	Becker, White & Edwards (1991)
4.85	$1.381 \pm 0.138$	White & Becker (1992)
4.85	$1.16 \pm 0.1$	Wallace, Landecker & Taylor (1997)
10.55	$0.95 \pm 0.05$	Wallace, Landecker & Taylor (1997)

much flatter spectrum than previously measured. This flat spectrum is also evident across the AMI SA band (Table 13).

Re-fitting the 327-MHz WSRT data of Taylor et al. (1996) we find an integrated flux density of  $0.77 \pm 0.08 \text{ Jy}$  towards G84.9+0.5, significantly lower than the previously measured value of  $S_i = 1.22 \pm 0.13 \text{ Jy}$  (Taylor, Wallace & Goss 1992). This implies that G84.9+0.5 is indeed an HII region rather than a SNR; a result which agrees with the conclusion of Foster et al. (2007) based on their radio recombination line data and also with the lack of polarized emission seen towards this object (Kothes et al. 2006).

**Table 8.** Integrated flux densities from the literature for G67.7+1.8.

$\nu/\text{GHz}$	$S_i/\text{Jy}$	Reference
0.327	$1.88 \pm 0.08$	Taylor, Wallace & Goss (1992)
1.42	$0.72 \pm 0.07$	Fürst et al. (1990)
3.90	$0.60 \pm 0.10$	Trushkin (1996)
4.85	$0.42 \pm 0.05$	Taylor, Wallace & Goss (1992)

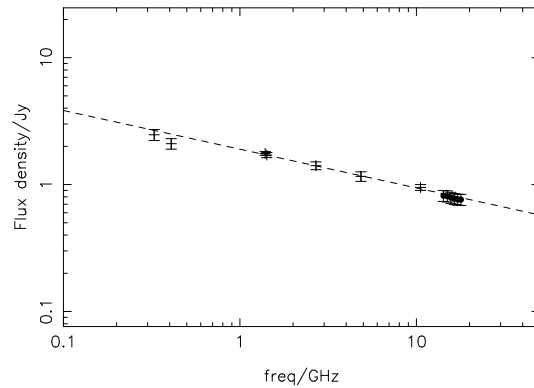
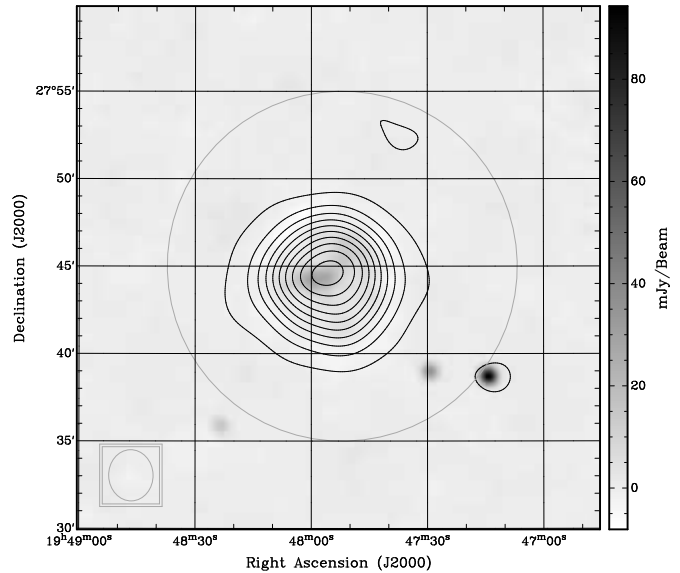


**Figure 8.** Above: Map of G63.7+1.1. AMI SA 16-GHz contours are overlaid on a NVSS 1.4-GHz greyscale image. Contours and annotations are as in Fig. 1. The peak level is  $153 \text{ mJy beam}^{-1}$ . Below: Radio spectrum of G63.7+1.1. Integrated flux densities taken from the literature (Table 7) are shown as crosses, and those from AMI SA (Table 12) are shown as filled circles. The best-fitting power-law, with  $\alpha = 0.30$ , is shown as a dashed line.

**Table 9.** Integrated flux densities from the literature for G74.9+1.2.

$\nu/\text{GHz}$	$S_i/\text{Jy}$	Reference
0.408	$11.6 \pm 0.4$	Wendker, Higgs & Landecker (1991)
0.408	$13.3 \pm 0.8$	Pineault & Chastenay (1990)
0.61	$9.1 \pm 1.2$	Weiler & Shaver (1978)
1.42	$7.2 \pm 0.3$	Pineault & Chastenay (1990)
1.415	$8.0 \pm 1.5$	Duin et al. (1975)
1.415	$8.7 \pm 1.2$	Weiler & Shaver (1978)
2.695	$7.6 \pm 0.5$	Geldzahler, Pauls & Salter (1980)
4.80	$7.5 \pm 0.7$	Wendker, Higgs & Landecker (1991)
4.995	$5.6 \pm 1.3$	Weiler & Shaver (1978)
8.35	$4.89 \pm 0.50$	Langston et al. (2000)
10.69	$4.8 \pm 1.2$	Green, Baker & Landecker (1975)
14.35	$2.47 \pm 0.20$	Langston et al. (2000)
32.0	$1.47 \pm 0.19$	Morsi & Reich (1987)
84.2	$0.6 \pm 0.1$	Salter et al. (1989)



**Table 12.** AMI SA I+Q flux densities for less well-studied SNR. Above: corrected for flux loss, where possible; below: original flux densities for those sources which undergo a flux loss correction.

Name	Freq. (GHz)					
	14.2 (Jy)	15.0 (Jy)	15.7 (Jy)	16.4 (Jy)	17.1 (Jy)	17.9 (Jy)
G54-1+0.3 <sup>a</sup>	0.340 ± 0.034	0.324 ± 0.032	0.281 ± 0.028	0.273 ± 0.027	0.261 ± 0.026	0.251 ± 0.025
G57-2+0.8 <sup>a</sup>	0.284 ± 0.033	0.271 ± 0.031	0.252 ± 0.028	0.223 ± 0.026	0.228 ± 0.026	0.228 ± 0.025
G63-7+1.1 <sup>b</sup>	0.818 ± 0.082	0.810 ± 0.081	0.790 ± 0.079	0.773 ± 0.077	0.764 ± 0.076	0.761 ± 0.076
G67-7+1.8 <sup>c</sup>	0.191 ± 0.019	0.170 ± 0.017	0.169 ± 0.017	0.148 ± 0.015	0.158 ± 0.015	0.163 ± 0.016
G74-9+1.2 <sup>c</sup>	2.26 ± 0.23	2.31 ± 0.23	2.26 ± 0.23	2.11 ± 0.21	2.04 ± 0.20	1.96 ± 0.20
G76-9+1.0 <sup>c</sup>	0.191 ± 0.019	0.170 ± 0.016	0.170 ± 0.016	0.168 ± 0.016	0.171 ± 0.016	0.154 ± 0.011
G84-9+0.5 <sup>d</sup>	–	0.526 ± 0.062	0.562 ± 0.058	0.532 ± 0.058	0.540 ± 0.055	–
G63-7+1.1	0.605 ± 0.030	0.591 ± 0.030	0.569 ± 0.029	0.549 ± 0.028	0.535 ± 0.027	0.525 ± 0.026
G67-7+1.8	–	–	–	–	0.148 ± 0.009	–
G74-9+1.2	1.44 ± 0.09	1.38 ± 0.07	1.36 ± 0.07	1.22 ± 0.06	1.14 ± 0.06	1.01 ± 0.10
G76-9+1.0	0.191 ± 0.010	0.162 ± 0.008	0.160 ± 0.008	0.155 ± 0.008	0.156 ± 0.08	0.142 ± 0.011

<sup>a</sup>Uncorrected for flux loss; complex region with no CGPS coverage.

<sup>b</sup>Corrected for flux loss using a Gaussian model.

<sup>c</sup>Corrected for flux loss using CGPS data.

<sup>d</sup>Flux loss correction smaller than other errors, so not included.

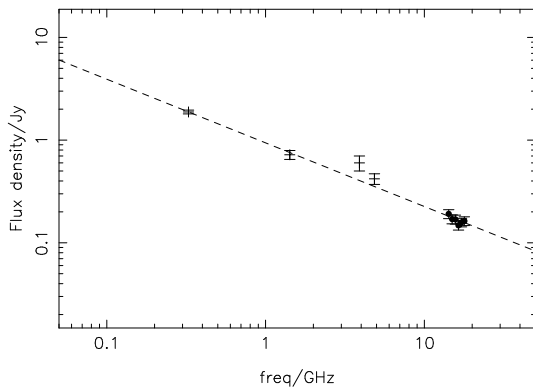
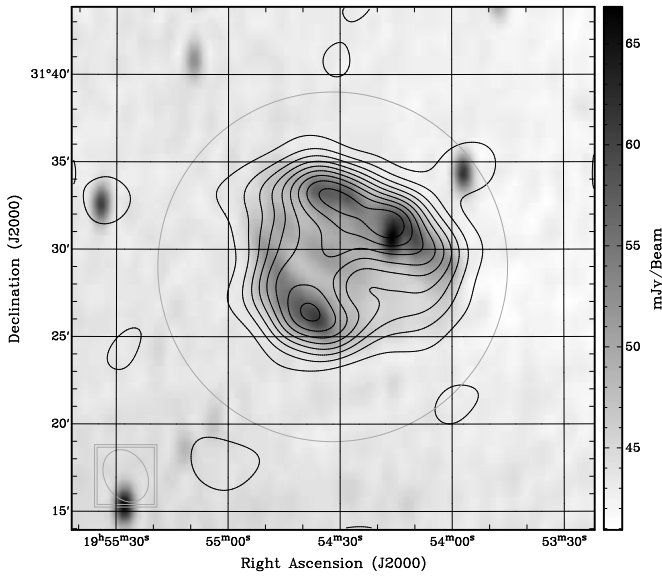


**Figure 9.** Above: Map of G67-7+1.8. AMI SA 16-GHz contours are overlaid on a CGPS 1.4-GHz greyscale image. Contours and annotations are as in Fig. 3. The peak level is 17.3 mJy beam<sup>-1</sup>. Below: Radio spectrum of G67-7+1.8. Integrated flux densities taken from the literature (Table 8) are shown as crosses, and those from AMI SA (Table 12) are shown as filled circles. The best-fitting power-law, with  $\alpha = 0.62$ , is shown as a dashed line.

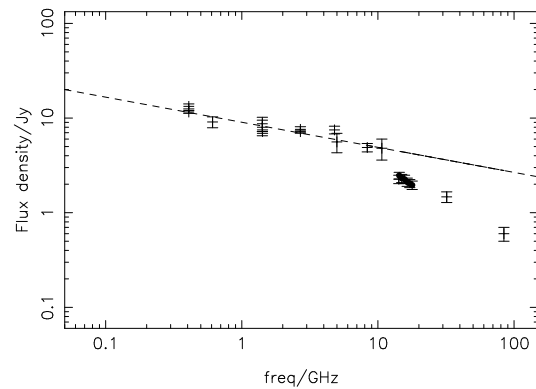
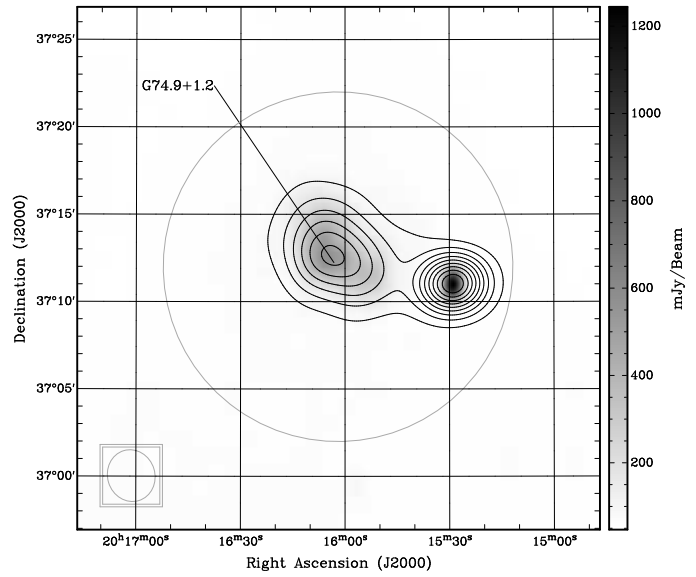


**Figure 10.** Above: Map of G74-9+1.2. AMI SA 16-GHz contours are overlaid on a CGPS 1.4-GHz greyscale image. Contours and annotations are as in Fig. 3. The peak level is 1.38 Jy beam<sup>-1</sup>. Below: Radio spectrum of G74-9+1.2. Integrated flux densities taken from the literature (Table 9) are shown as crosses, and those from AMI SA (Table 12) are shown as filled circles. The best-fitting power-law to the data below 12 GHz, with  $\alpha = 0.26$ , is shown as a dashed line.

**Table 10.** Integrated flux densities from the literature for G76-9+1-0.

$\nu$ /GHz	$S_\nu$ /Jy	Reference
0.232	$1.4 \pm 0.4$	Landecker et al. (1997)
0.327	$1.4 \pm 0.1$	Landecker et al. (1997)
0.327	$2.03 \pm 0.30$	Taylor, Wallace & Goss (1992)
0.408	$2.3 \pm 0.2$	Kothes et al. (2006)
0.408	$2.89 \pm 0.20$	Landecker, Higgs & Wendker (1993)
1.408	$1.70 \pm 0.20$	Landecker, Higgs & Wendker (1993)
1.42	$1.35 \pm 0.07$	Kothes et al. (2006)
1.49	$1.80 \pm 0.20$	Landecker, Higgs & Wendker (1993)
2.695	$0.90 \pm 0.09$	Landecker, Higgs & Wendker (1993)
4.80	$0.63 \pm 0.03$	Landecker, Higgs & Wendker (1993)
4.85	$0.44 \pm 0.01$	Taylor, Wallace & Goss (1992)
4.85	$0.466 \pm 0.028$	Gregory & Condon (1991)

**Table 11.** Integrated flux densities from the literature for G84-9+0-5.

$\nu$ /GHz	$S_\nu$ /Jy	Reference
0.151	$0.917 \pm 0.110$	Vessey & Green (1998)
0.232	$0.63 \pm 0.15$	Zhang et al. (1997)
0.327	$0.769 \pm 0.077$	This work, from the data of Taylor, Wallace & Goss (1992)
0.408	$0.700 \pm 0.08$	Kothes & Dougherty (2007)
1.42	$0.77 \pm 0.22$	Kothes & Dougherty (2007)
4.85	$0.517 \pm 0.052$	Gregory et al. (1996)

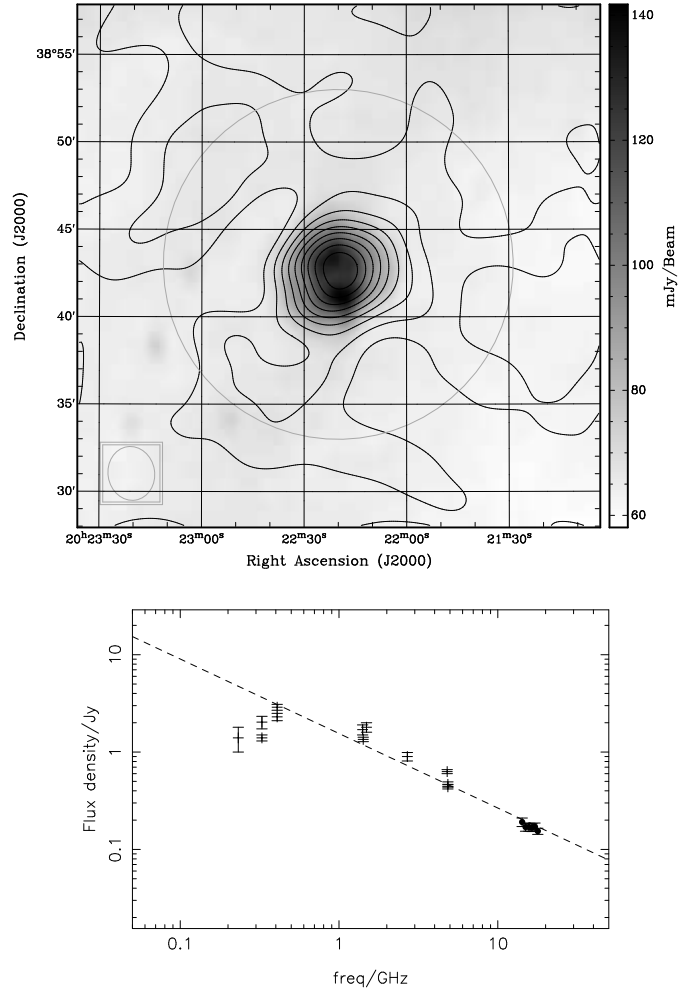
## 6 CONCLUSIONS

New observations in six channels spanning 14.2–17.9 GHz have improved our knowledge of the spectral behaviour of eight supernova remnants in the northern sky. Observations made of well-studied remnants confirm that AMI SA is measuring flux densities accurately and our flux loss measurements and fitting methods are correct. For those sources for which a flux loss correction was made, Table 13 gives an interpolated flux density and spectral index from the AMI data alone. The errors on the indices are relatively large, because of the limited frequency coverage of the telescope, but all values are consistent within one sigma with those calculated from the literature, except in the case of G74-9+1-2, as our measurements lie above the spectral break frequency of 11 GHz. We detect no anomalous excess emission from the observed SNRs, implying there is no spinning dust present. G54-1+0-3 shows a possible break in the AMI SA band but, due to changes in large-scale structure over AMI SA’s frequency coverage, we will need data at higher frequencies to provide a definite answer.

**Table 13.** AMI SA I+Q interpolated 16 GHz flux densities and estimated spectral indices, calculated from the AMI SA data in Tables 12 and 4 for sources for which a flux correction has been made.

Name	$S_{16\text{GHz}}$ (Jy)	$\alpha$
G63-7+1-1	$0.786^{+0.867}_{-0.412}$	$0.34 \pm 0.24$
G67-7+1-8	$0.165^{+0.162}_{-0.082}$	$0.76 \pm 0.25$
G74-9+1-2*	$2.189^{+1.928}_{-1.025}$	$1.00 \pm 0.23$
G76-9+1-0	$0.174^{+0.123}_{-0.073}$	$0.99 \pm 0.19$
G84-9+0-5	$0.533^{+0.383}_{-0.223}$	$-0.03 \pm 0.23$
G120-1+1-4	$10.76^{+8.96}_{-4.89}$	$0.99 \pm 0.19$
G130-7+3-1	$23.97^{+14.98}_{-9.22}$	$0.37 \pm 0.18$

\* Fit to data above 11 GHz.

**Figure 11.** Above: Map of G76-9+1-0. AMI SA 16-GHz contours are overlaid on a CGPS 1.4-GHz greyscale image. Contours and annotations are as in Fig. 3. The peak level is  $46.6 \text{ mJy beam}^{-1}$ . Below: Radio spectrum of G76-9+1-0. Integrated flux densities taken from the literature (Table 10) are shown as crosses, and those from AMI SA (Table 12) are shown as filled circles. The best-fitting power-law to the data above 1 GHz, with  $\alpha = 0.75$ , is shown as a dashed line.

## ACKNOWLEDGMENTS

We thank the whole AMI team for their invaluable assistance in the construction, commissioning and operation of AMI. AMI is supported by the STFC. NHW and MLD acknowledge the support of PPARC/STFC studentships.

## REFERENCES

- Aller H. D. & Reynolds S. P. 1985, *ApJ*, 293, L73  
 Altenhoff W. J., Downes D., Pauls T., Schraml J., 1979, *A&AS*, 35, 23  
 AMI Consortium: Scaife A., et al., 2007, *MNRAS*, 377, L69  
 AMI Consortium: Zwart J. T. L. et al., 2008, *MNRAS* in press, pre-print (astro-ph/0807.2469)  
 Baars J. W. M., Genzel R., Pauliny-Toth I. I. K., Witzel A., 1977, *A&A*, 61, 99  
 Becker R. H., White R. L., Edwards A. L., 1991, *ApJS*, 75, 1  
 Bock D. C.-J., Gaensler B. M., 2005, *ApJ*, 626, 343

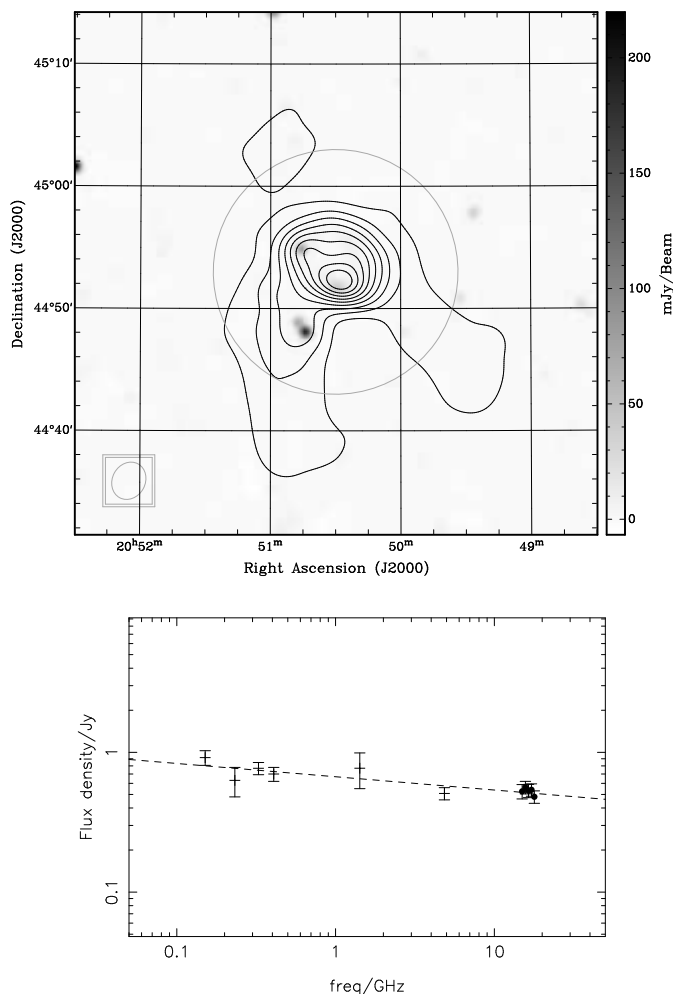


**Figure 12.** Above: Map of G84.9+0.5. AMI SA 16-GHz contours are overlaid on a NVSS 1.4-GHz greyscale image. Contours are as in Fig. 3. The peak level is  $158 \text{ mJy beam}^{-1}$ . Below: Radio spectrum of G84.9+0.5. Integrated flux densities taken from the literature (Table 11) are shown as crosses, and those from AMI SA (Table 12) are shown as filled circles. The best-fitting power-law, with  $\alpha = 0.08$ , is shown as a dashed line.

Boland J. W., Hollinger J. P., Mayer C. H., McCullough T. P. 1966, *ApJ*, 144, 437  
 Browne I. W. A., Wilkinson P. N., Patnaik A. R., Wrobel J. M., 1998, *MNRAS*, 293, 257  
 Caswell J. L., Haynes R. F., 1987, *A&A*, 171, 261  
 Chini R., Kruegel E., Wargau W., 1987, *A&A*, 181, 378  
 Condon J. J., Broderick J. J., Seielstad G. A., 1989, *AJ*, 97, 1064  
 Condon J. J., Cotton W. D., Greisen E. W., Yin Q. F., Perley R. A., Taylor G. B., Broderick J. J., 1998, *AJ*, 115, 1693  
 Duin R. M., Israel F. P., Dickel J. R., Seaquist E. R., 1975, *A&A*, 38, 461  
 Fesen R. et al., 2008, *ApJS*, 174, 379F  
 Foster T. J., Kothes R., Kerton C. R., Arvidsson K., 2007, *ApJ*, 667, 248  
 Fürst E., Reich W., Reich P., Reif K., 1990, *A&AS*, 85, 805  
 Geldzahler B. J., Pauls T., Salter C. J., 1980, *A&A*, 84, 237  
 Gotthelf et al, 2007 *ApJ*, 654, 267G  
 Green D. A., 1986, *MNRAS*, 218, 533  
 Green D. A., 2004, *BASI*, 32, 335  
 Green D. A., 2007, *BASI*, 35, 77

Green A. J., Baker J. R., Landecker T. L., 1975, *A&A*, 44, 187  
 Green D. A., Scheuer P. A. G., 1992, *MNRAS*, 258, 833  
 Green D. A., Tuffs R. J., Popescu C. C., 2004, *MNRAS*, 355, 1315  
 Gregory P. C., Condon J. J., 1991, *ApJS*, 75, 1011  
 Gregory P. C., Scott W. K., Douglas K., Condon J. J., 1996, *ApJS*, 103, 427  
 Griffith M., Langston G., Heflin M., Conner S., Lehar J., Burke B., 1990, *ApJS*, 74, 129  
 Handa T., Sofue Y., Nakai N., Hirabayashi H., Inoue M., 1987, *PASJ*, 39, 709  
 Katz-Stone D. M., Kassim N. E., Lazio T. J. W., O'Donnell R., 2000, *ApJ*, 529, 453  
 Klein U., Emerson D. T., Haslam C. G. T., Salter C. J., 1979, *A&A*, 76, 120  
 Kneissl R., Jones M. E., Saunders R., Eke V. R., Lasenby A. N., Grainge K., Cotter G., 2001, *MNRAS*, 328, 783  
 Kneissl R., Jones M. E., 2002, *ASPC*, 268, 121  
 Kothes R., Fedotov K., Foster T. J., & Uyaniker B. 2006, *AAp*, 457, 1081  
 Kothes R., Dougherty S. M., 2007, *A&A*, 468, 993  
 Kovalenko A. V., Pynzar A. V., Udalt'sov V. A., 1994, *ARep*, 38, 95  
 Landecker T. L., Caswell J. L., 1983, *AJ*, 88, 1810  
 Landecker T. L., Higgs L. A., Wendker H. J., 1993, *A&A*, 276, 522  
 Landecker T. L., Zheng Y., Zhang X., Higgs L. A., 1997, *A&AS*, 123, 199  
 Langston G., Minter A., D'Addario L., Eberhardt K., Koski K., Zuber J., 2000, *AJ*, 119, 2801  
 Lockman F. J. 1989, *ApJS*, 71, 469  
 Mason B. S., Leitch E. M., Myers S. T., Cartwright J. K., Readhead A. C. S., 1999, *AJ*, 118, 2908  
 Metropolis N., Rosenbluth A. W., Rosenbluth M. N., Teller E., 1953, *Journal of Chemical Physics*, 21, 1087-1092  
 Morsi H. W., Reich W., 1987, *A&AS*, 71, 189  
 O'Sullivan C., Green D. A., 1999, *MNRAS*, 303, 575  
 Patnaik A. R., Browne I. W. A., Wilkinson P. N., Wrobel J. M., 1992, *MNRAS*, 254, 655  
 Pineault S., Chastenay P., 1990, *MNRAS*, 246, 169  
 Rees N., 1990, *MNRAS*, 243, 637  
 Reich W., Fürst E., Haslam C. G. T., Steffen P., Reif K., 1984, *A&AS*, 58, 197  
 Reich W., Fürst E., Altenhoff W. J., Reich P., Junkes N., 1985, *A&A*, 151, L10  
 Reynolds S. P., Ellison D. C., 1992, *ApJ*, 399, L75  
 Salter C. J., Reynolds S. P., Hogg D. E., Payne J. M., Rhodes P. J., 1989, *ApJ*, 338, 171  
 Sieber W., Seiradakis J. H., 1984, *A&A*, 130, 257  
 Stephenson F. R., Green D. A., 2002, "Historical Supernovae and their Remnants", (OUP)  
 Taylor A. R., Goss W. M., Coleman P. H., van Leeuwen J., Wallace B. J., 1996, *ApJS*, 107, 239  
 Taylor A. R., Wallace B. J., Goss W. M., 1992, *AJ*, 103, 931  
 Tian W. W., Leahy D. A., 2005, *A&A*, 436, 187  
 Tian W. W., Leahy D. A., 2006, *A&A*, 451, 991  
 Trushkin S. A., Vitkoskij V. V., Nizhelskij N. A., 1987, *AISAO*, 25, 84  
 Trushkin S. A., 1996, *BSAO*, 41, 64  
 Urošević D., Pannuti T. G., Leahy D., 2007, *ApJ*, 655, L41  
 Velusamy T., Becker R. H., 1988, *AJ*, 95, 1162  
 Vessey S. J. & Green D. A. 1998, *MNRAS*, 294, 607  
 Vinyaikin E. N., 2007, *ARep*, 51, 570  
 Wallace B. J., Landecker T. L., Taylor A. R., 1997, *AJ*, 114, 2068

- Weiler K. W., Shaver P. A., 1978, *A&A*, 70, 389  
Wendker H. J., Higgs L. A., Landecker T. L., 1991, *A&A*, 241, 551  
White R. L., Becker R. H., 1992, *ApJS*, 79, 331  
Wilkinson P. N., Browne I. W. A., Patnaik A. R., Wrobel J. M.,  
Sorathia B., 1998, *MNRAS*, 300, 790  
Zhang X., Zheng Y., Chen H., Wang S., Cao A., Peng B., Nan R.  
1997, *A&AS*, 121, 59

This paper has been typeset from a  $\text{T}_{\text{E}}\text{X}/\text{L}^{\text{A}}\text{T}_{\text{E}}\text{X}$  file prepared by the author.